Structure *14*, 331–343, February 2006 ©2006 Elsevier Ltd All rights reserved DOI 10.1016/j.str.2005.11.010

Crystal Structures of U8 snoRNA Decapping Nudix Hydrolase, X29, and Its Metal and Cap Complexes

J. Neel Scarsdale,[1,3] Brenda A. Peculis,[2,4] and H. Tonie Wright[1,5,*]
[1] Department of Biochemistry and
Institute of Structural Biology and Drug Discovery
Virginia Commonwealth University
800 E. Leigh Street
Suite 212
Richmond, Virginia 23219
[2] Department of Biochemistry
117 Schweitzer Hall
University of Missouri, Columbia
Columbia, Missouri 65211

Summary

X29, a 25 kDa Nudix hydrolase from *Xenopus laevis* that cleaves 5′ caps from U8 snoRNA, crystallizes as a homodimeric apoenzyme. Manganese binds crystals of apo-X29 to form holo-X29 only in the presence of nucleot(s)ide. Structural changes in X29 on nucleot(s)ide-assisted Mn^{+2} uptake account for the observed cooperativity of metal binding. Structures of X29 with GTP or m^7GpppA show a different mode of ligand binding from that of other cap binding proteins and suggest a possible three- or four-metal Nudix reaction mechanism. The X29 dimer has no known RNA binding motif, but its striking surface dipolarity and unique structural features create a plausible RNA binding channel on the positive face of the protein. Because U8 snoRNP is essential for accumulation of mature 5.8S and 28S rRNA in vertebrate ribosome biogenesis, and cap structures are required for U8 stability in vivo, X29 could profoundly influence this fundamental cellular pathway.

Introduction

Eukaryotic ribosome biogenesis requires assembly of precursor rRNA with factors that associate stably (i.e., ribosomal proteins) or transiently (helicases, endonucleases, exonucleases, and the snoRNPs) (Venema and Tollervey, 1999; Warner, 1990; Woolford, 1991). Together, these factors carry out processing and modification events, most of which probably occur cotranscriptionally. Whereas most of the small nucleolar ribonucleoprotein particles (snoRNP) function as "guide RNAs" to direct site-specific modifications of pre-rRNAs (Peculis, 1997; Peculis and Mount, 1996; Weinstein and Steitz, 1999), a handful of snoRNPs, including U8 snoRNP, mediate pre-rRNA cleavage steps (Maxwell and Fournier, 1995; Peculis and Steitz, 1993). Maturation of the large ribosomal subunit RNAs (5.8S and 28S rRNAs) in vertebrates requires U8 snoRNP. The U8 small nucleolar RNA (snoRNA) component of the U8 snoRNP is independently transcribed by PolII (Peculis et al., 2001), has a hypermethylated 2,2,7-trimethylguanosine (m^{227}G) 5′ cap (Peculis and Steitz, 1993; Tyc and Steitz, 1989), and encodes the canonical Box C and Box D sequences that together form a K turn (Watkins et al., 2000), which is required for binding the four core C/D box proteins: snu13/15.5 kDa, fibrillarin (Nop1 in yeast), Nop56p, and Nop58p (Watkins et al., 2002).

We previously reported that X29 protein binds U8 snoRNA with high affinity and specificity (Tomasevic and Peculis, 1999). X29 has a sequence motif characteristic of the Nudix hydrolase enzyme family, whose members catalyze hydrolysis of small nucleot(s)ides (Bessman et al., 1996; Ghosh et al., 2004; Mildvan et al., 2005). In vitro, X29 removes 7-methylguanosine-5′-diphosphate (m^7GDP) and m^{227}GDP from the 5′ end of U8 snoRNA in a metal-dependent manner (Ghosh et al., 2004), consistent with its classification as a Nudix hydrolase (Figure 1). The cap-cleaving activity of X29 is similar to the cytosolic human mRNA decapping enzyme hDcp2, which also carries a Nudix domain essential for decapping activity (Wang et al., 2002). Dcp2 releases m^7GDP from capped, deadenylated mRNA, leaving 5′-monophosphorylated mRNA, which is a target for degradation by exonucleases. In yeast, Dcp2p appears to be the catalytic component of a complex with Dcp1p (She et al., 2004) and probably several other proteins. A "scavenger" cap-cleaving enzyme, DcpS, releases m^7GMP from terminal products of capped mRNA that has been degraded from the 3′ end, leaving 5′-diphosphate caps or mRNA fragments. DcpS has no Nudix domain and its structure (Gu et al., 2004) is unrelated to X29. X29 was the first nuclear decapping enzyme to be identified and characterized, and its tight association with U8 snoRNA implies a unique role in the in vivo stability of U8 and possibly other small nuclear RNAs.

We report here the crystal structure of X29 in its apo- (no bound metal) and holo- (with bound Mn^{+2}) forms. We have also determined the structures of the X29 homodimer in complex with GTP (pppG) and m^7GpppA, which correspond to part or all of the 5′ terminus of U8 snoRNA, respectively. These structures confirm that X29 has the characteristic Nudix fold that we previously inferred from sequence data and functional biochemical analysis. However, the structure of X29 shows extensions of surface loops and chain termini and a highly dipolar surface charge distribution that distinguish it from the structures of Nudix enzymes specific for small substrates.

X29 crystals require the presence of a nucleot(s)ide for metal binding, and in its complex with m^7GpppA, X29 has three or four Mn^{+2} in each active site of the dimer. Mn^{+2} binding to X29 is cooperative and the structural basis for the requirement of nucleot(s)ide for metal binding to occur and the cooperativity of this binding can be understood from the structures described here. The Mn^{+2} positions in the X29-m^7GpppA complex structure suggest that the metals function both in substrate binding and catalysis through a mechanism similar to that

*Correspondence: xrdproc@hsc.vcu.edu
[3] Lab address: http://www.vcu.edu/biochem/faculty/scarsdale.shtml
[4] Lab address: http://biochem.missouri.edu/bpeculis.php
[5] Lab address: http://www.vcu.edu/biochem/faculty/wright.shtml

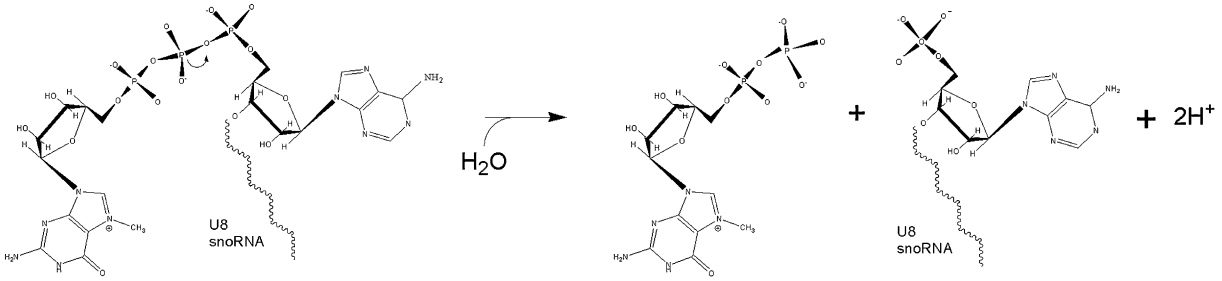

Figure 1. Overall Reaction Catalyzed by X29

hypothesized for other Nudix hydrolases (Mildvan et al., 2005). These results further expand the repertoire of Nudix hydrolase specificity and function (Gabelli et al., 2001) and show how this versatile family of enzymes has evolved structurally and mechanistically to play a role in RNA metabolism.

Results

Structure of Apo-X29

The crystal structure of apo-X29 was determined to 2.1 Å resolution with multiple isomorphous replacement from three soaked heavy atom derivatives with anomalous dispersion data from one of these (see Experimental Procedures). Electron density near the amino terminus is broken at several places in the A monomer, but mostly contiguous in the B chain; both monomers lack electron density for the first 17–18 amino acids.

The asymmetric unit of apo-X29 consists of a homodimer of X29 monomers which are virtually identical in backbone conformation and show the expected Nudix fold. Each X29 monomer consists of two domains (Figure 2A, gold and green) of comparable size defined by noncontiguous polypeptide segments. One domain (gold) carries the Nudix motif (Figure 2B, red) and the other domain (Figure 2A, green) contributes most of the monomer-monomer contact interface and presents three surface extensions (Figure 2B, magenta) that are

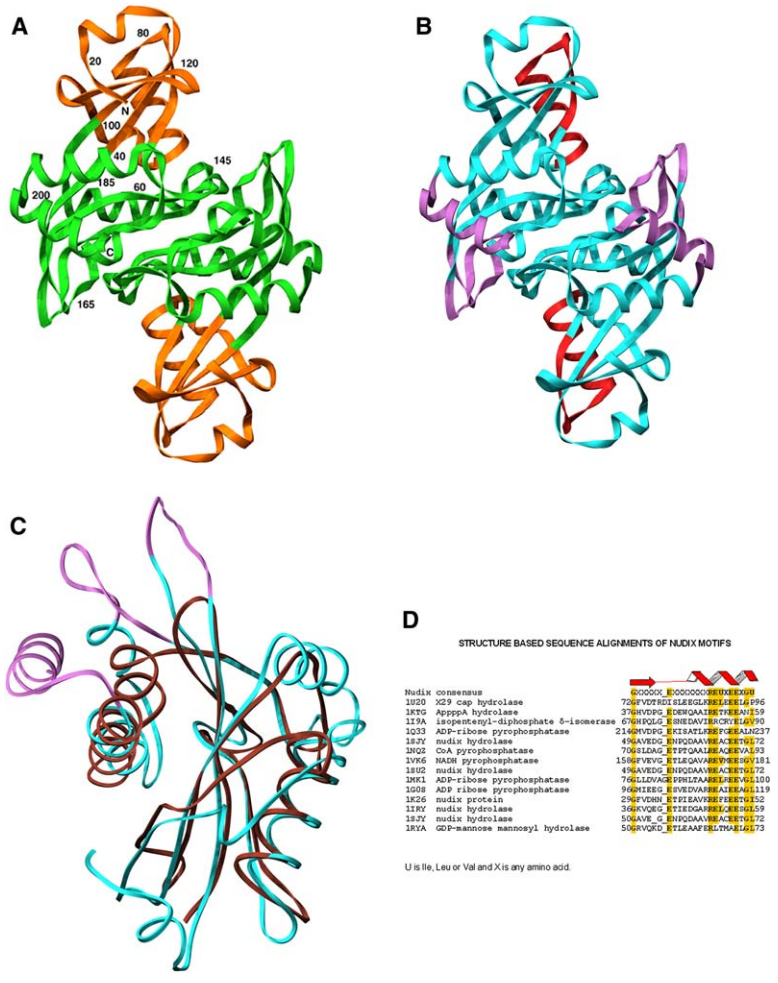

Figure 2. Polypeptide Backbone Folds and Features of X29 and Relationship to Other Nudix Hydrolases

(A) Ribbon diagram of the X29 dimer viewed down the noncrystallographic dyad axis showing the two domains (gold and green) in each monomer. The gold domain carries most of the functional groups of the active site and the green forms the interface of the monomers and provides surface extensions that define one side of the putative RNA binding channel of the opposed monomer.

(B) Ribbon diagram of the X29 dimer showing the Nudix motif (red) and the loop and carboxy-terminal extensions (magenta) that define one side of the RNA binding channel of the opposite subunit and distinguish X29 from other Nudix hydrolases.

(C) Backbone ribbon diagram of the X29 monomer (cyan) overlaid on that of diadenosine tetraphosphate hydrolase (RCSB accession number 1KTG) (brown) from *Caenorhabditis elegans* showing the extensions in X29 (magenta and in [B]) projecting beyond those of 1KTG.

(D) Sequence alignment of Nudix domain sequences for dimeric Nudix hydrolases of known structure (RCSB accession numbers on left). Conserved residues matching the Nudix motif are highlighted in gold. Sequence numbers for each Nudix domain are shown at the beginning and end. Arrow and helix (red) show strand and helix of the Nudix motif secondary structure displayed in red in (B).

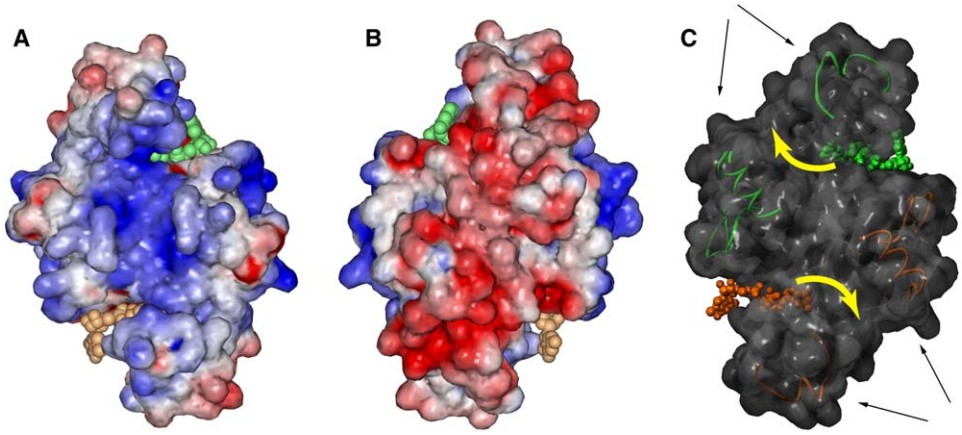

Figure 3. Surface Charge Distribution of Opposite Faces of X29

Blue indicates regions of positive surface charge and red indicates negative, contoured at ± 5kt cutoff, respectively. Overlaid ribbon in (C) shows extensions (black arrow pointers) that define the two sides of the inferred RNA binding channel, which is indicated by yellow arrows. Active sites of each monomer are occupied by m^7GpppA (gold and green ball-and-stick). Views are down the dyad axis.

unique to X29 relative to other Nudix hydrolases. The X29 monomer fold resembles that of other Nudix hydrolases as shown in Figure 2C. The X29 backbone (cyan) has a closely similar fold to AppppA Nudix hydrolase (Research Collaboratory for Structural Bioinformatics [RCSB] accession number 1KTG) from *C. elegans* (brown) (Bailey et al., 2002), with the conspicuous exception of the surface extensions (magenta). X29 shows less congruence with other Nudix hydrolase structures. Although they share a similar fold, the Nudix hydrolase structures show variable degrees of congruence and correspondence of secondary structure elements among their main chains, except for the Nudix motif of about 22 residues, which is highly conserved in structure. However, even this conserved motif shows only weak primary sequence similarity among members of this protein family (Figure 2D).

The X29 Dimer Interface and Surface Charge Distribution

The X29 monomers are associated across an extended contact surface of about 2500 $Å^2$ mediated by a trans-subunit β sheet and multiple hydrogen bond and hydrophobic contacts (Figure 2A). These intermonomer interactions are unique among known dimeric Nudix structures, which show wide variation in the locations and types of their interfaces. The Mn^{+2} and cap binding functional groups (see below) of each active site lie in one monomer chain, with the exception of Phe49, which is contributed from the opposing monomer of the dimer.

A striking feature of the X29 dimer structure is a strong dipolarity of surface charge (Figure 3). The long axes of the positively and negatively charged zones on each face are oriented approximately perpendicular to each other. The two active sites of the homodimer each lie near the boundary between these two oppositely charged surfaces and are related by the local dyad axis centered perpendicular to the charged face. The RNA substrate bound in the active site is inferred to lie on the positively charged face (Figure 3C, yellow arrows), and this inference is consistent with the orientation of the m^7GpppA ligand observed in each active site (see below).

Metal Binding to Apo-X29 in the Presence of m^7G Nucleot(s)ides

There is no electron density for metals in the structure determined for recombinant X29 (apo-X29) from crystals grown in the absence of added metal. Soaks of apo-X29 crystals in solutions of Mn^{+2}, Mg^{+2}, alkali, alkali earth, transition metals, or lanthanides at concentrations up to 30 mM failed to yield detectable binding in these sites. The active site of each of the monomers in the asymmetric unit is fully accessible and not obstructed by any crystal contacts. Variation of pH of the soak solution from pH 6.0 to 9.0 did not induce metal binding. However, in the presence of m^7GTP, m^7GDP, and m^7G, we were able to confirm binding of Mn^{+2} (added as $MnCl_2$) in anomalous difference Fourier maps (see below). Surprisingly, none of the $2mF_o - dF_c$ or $mF_o - dF_c$ maps for these structures showed electron density for the nucleot(s)ide. For the m^7GTP and m^7GDP soaks with Mn^{+2}, additional density within bonding distance of the Mn^{+2} atoms in all but one of the subunits was interpreted as pyrophosphate, which was found to be a significant impurity (5%–10% by weight) in the m^7G nucleotides (but not the m^7G nucleoside) used in the soaks.

Each active site of the X29 dimer in these complexes has two or three Mn^{+2} atoms, but there is variation in the Mn^{+2} positions among the different structures (Table 1; Figure 4A). In the case of monomer A of the m^7G + Mn^{+2} soak, the two anomalous density peaks are too close to be present simultaneously and are inferred to be conditionally occupied sites. The ligands for the bound Mn^{+2} are the carboxylates of three glutamates (Glu89, Glu92, and Glu93) and the peptide carbonyl oxygen of Gly72 in the Nudix motif plus the carboxylate of Glu150. In the Mn^{+2} complexes formed in the presence of the two nucleotides (m^7GDP and m^7GTP), the putative pyrophosphate groups coordinate Mn^{+2} through their oxygens. The carboxylate ligands and the pyrophosphate coordinate Mn^{+2} pairs through both

Table 1. Crystal Structures of X29

Name	Soaking Conditions	Resolution (Å)	Ligands Present in Subunit	
			A	B
Native (apo)	—	2.10	—	—
Holo-(m^7G)	$m^7G + Mn^{+2}$	2.70	2[a] Mn^{+2}	3 Mn^{+2}
Holo-(m^7GDP)	$m^7GDP + Mn^{+2}$	2.60	3 Mn^{+2}, PP	2 Mn^{+2}
Holo-(m^7GTP)	$m^7GTP + Mn^{+2}$	2.45	3 Mn^{+2}, PP	2 Mn^{+2}, PP
pppG complex	$pppG + Mn^{+2}$	2.41	4 Mn^{+2}, GTP	4 Mn^{+2}, GTP
m^7GpppA complex	$m^7GpppA + Mn^{+2}$	2.10	4 Mn^{+2}, m^7GpppA	5[b] Mn^{+2}, m^7GpppA

[a] Conditional occupancy of these two sites.
[b] Two pairs of Mn^{+2} with conditional occupancy.

single oxygen and bridging interactions. The carboxylates of Glu89, Glu93, and Glu150 each simultaneously coordinate two Mn^{+2} with μ-1,1 or μ-1,3 geometry (Dismukes, 1996) in the syn configuration (Glusker et al., 2001).

Comparison of the structures of Mn^{+2}-bound X29 with apo-X29 shows that the only significant changes in structure accompanying Mn^{+2} binding are in the side chains of the glutamates. Glu150 undergoes the largest side chain reorientation in coordinating to two Mn^{+2} (Figure 4B); the other glutamate side chains show smaller changes in side chain dihedral angles. The observed change in orientation of the Glu150 side chain induced by binding of an initial Mn^{+2}, and its simultaneous coordination of a second Mn^{+2}, which in turn simultaneously coordinates a third Mn^{+2}, suggest a cooperative order for Mn^{+2} uptake through coordinate bridging of the ligand carboxylates of Glu89 and Glu93 to subsequent Mn^{+2}. To test this hypothesis, the efficiency of X29 decapping of U8 snoRNA was determined as a function of Mn^{+2} concentration in the range of 0–150 μM $MnCl_2$. The dependence of decapping efficiency on Mn^{+2} concentration is sigmoidal, indicating cooperativity in Mn^{+2} binding (Figure 4C). A Hill plot of these data gives a K_d of 38 μM and a Hill coefficient of n = 3 (Figure 4C, inset), consistent with the presence of three cooperatively bound Mn^{+2} atoms, which are coordinately complexed pairwise by protein carboxylates. One other Nudix hydrolase, the diadenosine pyrophosphatase from *Bartonella bacilliformis*, has been shown to take up Mn^{+2} cooperatively with a Hill coefficient of 3 (Conyers et al., 2000), but no crystal structure is yet available for this enzyme.

Structure of X29 Complexes with m^7GpppA and pppG in the Presence of Mn^{+2}

Structures were also determined for soaked complexes of X29 with pppG (Figure 5) or m^7GpppA (Figure 6) in the presence of Mn^{+2} (Table 1). Electron density for the pppG ligand in its complex is complete, but in the m^7GpppA complex, electron density for the adenine in both subunits is weak at N1, C2, and N3 of the purine rings, and there is incomplete electron density for the m^7G group on the surface. The pppG and m^7GpppA ligands occupy identical sites in the two complexes, but the occupancy of the latter is lower in monomer B than in A. The triphosphate groups each coordinate with three or four Mn^{+2} and make an ion pair with Arg63, but there is a small difference in position of the terminal P_γ and its coordinated Mn^{+2} in the pppG structure relative to that of m^7GpppA.

The G and A rings of pppG and m^7GpppA in their complexes are buried in a crevice and differ in conformation, the G of the pppG complex being anti and the A in the m^7GpppA complex syn. (The partial density for A in the m^7GpppA complex may reflect a mixture of the two conformations.) The G is hydrogen bonded through its protonated N1 to OE1 of Gln184, through its N2 amino group to the amido OD1 of Asn180, through its O6 to the peptide -NH- of Phe70 and through its N7 to a solvent. In the m^7GpppA structure, the A is hydrogen bonded through its N6 amino group to OE1 of Gln184 and through its N7 to the amido -NH2- of Asn180. His37 is coplanar with the G or A ring in both structures.

In the m^7GpppA complex structure, there is incomplete electron density for the m^7G ring in monomer A and no electron density for it in monomer B. This group is exposed to solvent, making very few protein contacts. The only significant interactions of the m^7G nucleoside part of m^7GpppA with the protein are through a bound Mn^{+2} coordinated to O1′ and O5′ of the m^7G ribose in the A site (Figures 4B and 6) and with Phe49 of the opposite monomer, which stacks on the nucleoside ribose. The possible importance of this interaction is discussed below.

The Mn^{+2} atoms in the pppG and m^7GpppA complexes of X29 range in coordination number from two to five and are generally in a distorted tetrahedral geometry. All but two of the inter-Mn^{+2} distances lie in the range of 3–6 Å observed for other dimanganese proteins (Glusker et al., 2001) (Table 2). In the B subunit of the X29-m^7GpppA complex, two inter-Mn^{+2} distances (Mn305-Mn305*) and (Mn306-Mn306*) are exceptionally short. This is very likely the result of conditional occupancy of each of the two sites in each pair, and the occupancy of each of these pairs is probably correlated.

The structure of the pppG complex is similar to that of the m^7GpppA complex, except that one of the Mn^{+2} of the triad is displaced, apparently as a consequence of the small movement of the terminal P_γ of the pppG ligand relative to the m^7GpppA structure. This displaced Mn^{+2} and the apparent alternate Mn^{+2} site(s) in monomer B of the m^7GpppA complex indicate that the Mn^{+2} positions are labile depending on the presence of ligand in the active site and its identity and conformation. It is also consistent with the broad distribution of Mn^{+2} positions in the structures of complexes soaked in the presence of m^7G nucleot(s)ides (Figure 4A). However, the

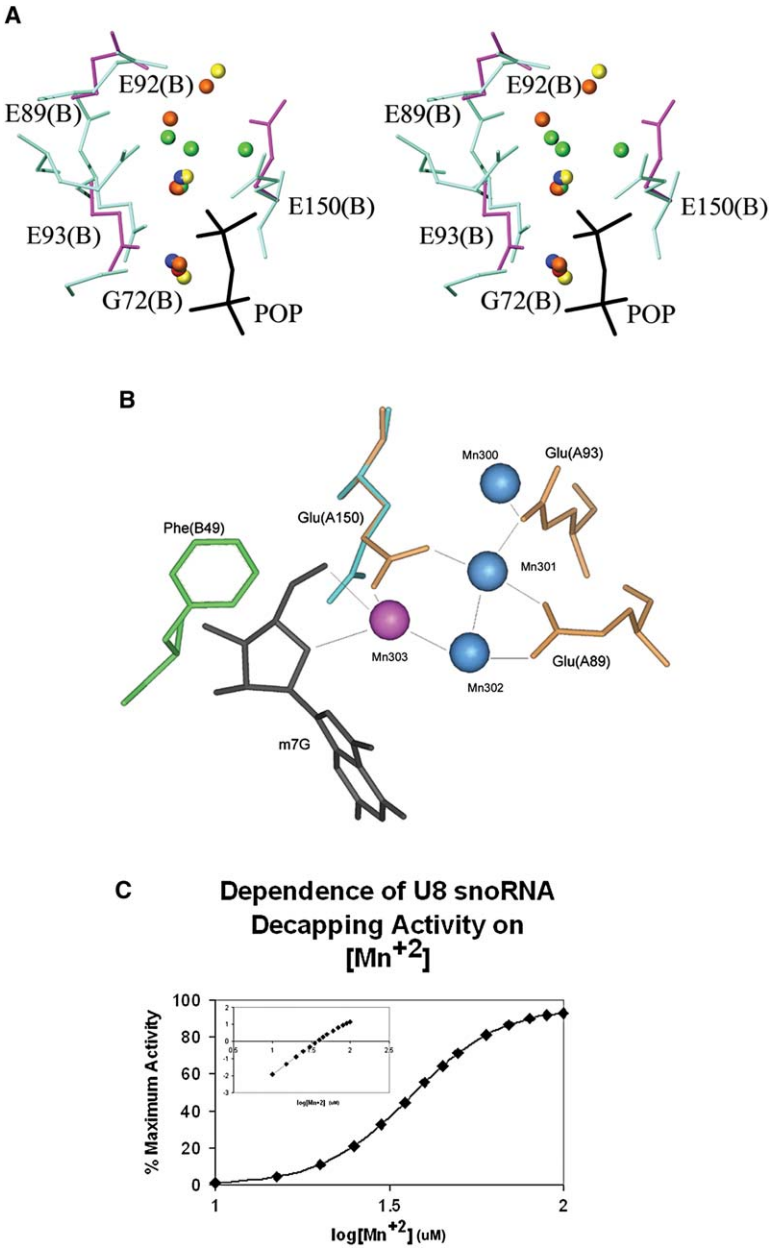

Figure 4. Mn^{+2} Positions in X29 Structures and Effects on X29 Decapping Activity

(A) Stereoview of a composite overlay of Mn^{+2} positions (balls) in the B subunit binding sites of all structures determined with Mn^{+2} present. Red, m^7G; blue, m^7GDP; yellow, m^7GTP; orange, pppG; green, m^7GpppA. Black stick model is pyrophosphate present in m^7GDP and m^7GTP soaks.

(B) Subunit A active site of m^7GpppA structure showing Glu150 side chain reorientation in the presence of a bound Mn^{+2} (magenta), which is coordinated to the m^7G nucleoside portion of the cap. Other Mn^{+2} are cyan. Mn301, Mn302, and Mn303 (monomer A) are the core triad centered on the P_β of m^7GpppA.

(C) Dependence of decapping activity on [$MnCl_2$] and the Hill plot (inset) derived from this binding activity curve.

inter-Mn^{+2} distances in the A subunit of the m^7GpppA complex structure and the observed occupancies are consistent with the presence of the Mn^{+2} triad in a majority of molecules in the crystal lattice (Table 2).

The Mn^{+2} triad plus the fourth Mn^{+2} in the A site of the m^7GpppA complex are liganded to the carboxylates of Glu89, Glu93, and Glu150 and to the peptide carbonyl of Gly72, as is observed in the structures of holo-X29 formed by soaking crystals with Mn^{+2} in the presence of m^7G nucleot(s)ides. These carboxylates form cross-bridges among the Mn^{+2}, which simultaneously make inner sphere interactions with the oxygens of the P_α-P_β pyrophosphoryl group of the pppG and m^7GpppA structures, and with pyrophosphate in the structures of holo-X29 formed in the presence of m^7GDP and m^7GTP (Table 2). While the structure of the Mn^{+2} triad is most consistent with an initial binding of an Mn^{+2} (Mn301 in A and Mn305 in B) to a reoriented Glu150 side chain carboxylate, followed by the two other Mn^{+2} of the triad, we cannot exclude the possibility that only two sites in the triad are occupied cooperatively. In this case, the Hill coefficient of 3 may reflect the uptake of the fourth Mn^{+2} (Mn300, Mn304) outside of the triad, which stabilizes the leaving group side of the substrate. Studies are underway to address this question.

RNA Binding Site

A survey of other known dimeric Nudix hydrolase structures shows that X29 is unique in having a strong dipolarity of surface charge. It is likely that the positive face of the X29 dimer is the dominant site of interaction of the U8 snoRNA substrate. If we assume simultaneous binding of RNA to each monomer of the dimer, a plausible path for the 5′ terminal residues of each RNA

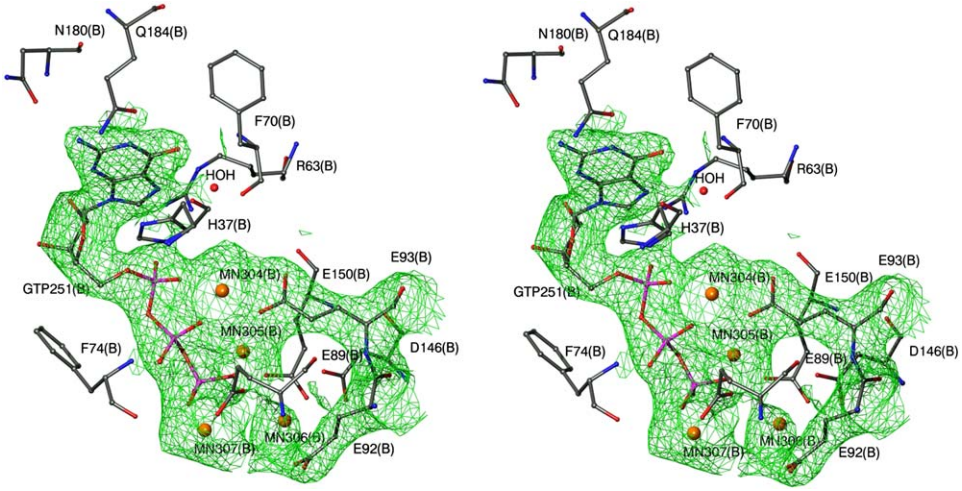

Figure 5. Stereoview of Electron Density for pppG Bound in Active Site of X29

Stereoview of electron density (contoured at 1σ) for pppG bound in the active site of X29. Electron density for some protein groups is omitted for clarity. Orange balls are Mn^{+2} atoms.

substrate can be extrapolated from the 3′ oxygen of the bound m^7GpppA in its complex with X29 (yellow arrows in Figure 3C). Each of these paths lies on the cationic surface of one monomer and extends to a length that could interact with at least five to six and as many as eight to ten single-strand nucleotides of the RNA substrate; because U8 has much secondary structure, the actual number of interacting nucleotides may be higher. Simultaneous binding of two RNA substrate molecules on the cationic face would bring them into proximity near the dyad axis, which would be electrostatically unfavorable, but not impossible. A stoichiometry of one U8 snoRNA per dimer is equally plausible, in which case the path of the RNA could extend across the two subunits. The stoichiometry of this complex in solution is the subject of ongoing experiments. The requirement for a minimal size/structure RNA substrate for efficient RNA binding to X29 indicates that the RNA makes an extended interaction with the X29 5′ terminus or that it has a specific higher order structure requiring distal interactions extending beyond the five to ten residues at the 5′ terminus (Ghosh et al., 2004; Tomasevic and Peculis, 1999).

Discussion

Mechanism of Cap Hydrolysis

The low level of sequence similarity among Nudix enzymes is consistent with the broad range of substrate specificities and variable number and identity of divalent metal ions observed in this enzyme family. This diversity further suggests there will be variations in the details of Nudix mechanisms. All Nudix mechanisms appear to involve nucleophilic substitution, most frequently but not exclusively at a phosphorus, and most require more than one divalent metal ion. These metal ions, in concert with a general base, play the essential roles of stabilizing the anionic substrate in its transition state and activating a water molecule to a nucleophilic species, which in the case of phosphate hydrolysis, axially attacks the phosphorus atom to form the pentacovalent trigonal bipyramid transition state (Lin et al., 1997). A metal, or other cationic group, is usually present at the active site to stabilize the leaving group of the reaction.

The structure of the m^7GpppA complex suggests a mechanism for the cleavage reaction mediated by

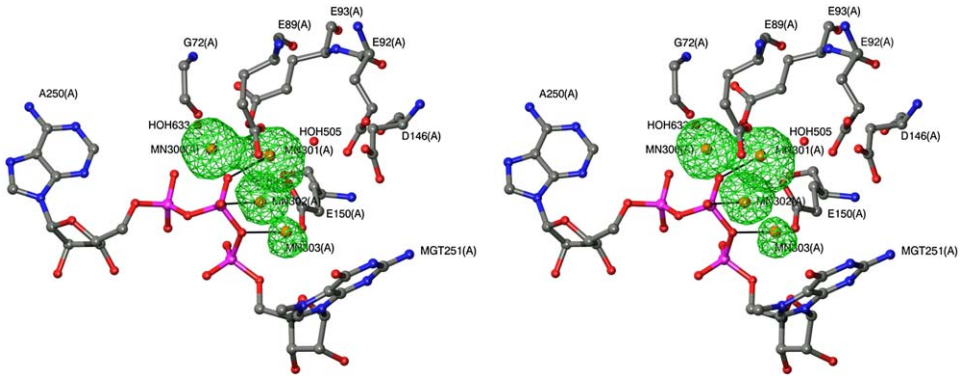

Figure 6. Stereoview of Bound m^7GpppA in Site A of the X29 Dimer

The coordination of the four Mn^{+2} atoms is shown with the electron density for the Mn^{+2} from the anomalous difference map contoured at 8σ. Coordination interactions of the Mn^{+2} triad and the target phosphoryl group are shown by black lines.

Table 2. Coordination, Occupancies, and Ligand Bond Distances (Å) for Mn^{+2} and m^7GpppA in the m^7GpppA-X29 Complex

Monomer A								Monomer B							
	N	Q	Mn300	Mn301	Mn302	Mn303		Mn304	Mn305	Mn305*	Mn306	Mn306*	Q	N	
Mn300	5	1.0											0.8	5	Mn304
Mn301	5	1.0	3.19					2.96					0.8	4	Mn305
Mn302	2	1.0		*3.74*					2.27				0.2	3	Mn305*
Mn303	3	0.5		*3.60*	*2.96*				3.47	4.22			0.3	3	Mn306
m^7GpppA		0.8							3.63	4.60	2.78		0.6	4–5	Mn306*
O1B					2.08								0.50		m^7GpppA
O2A			2.07					2.08				2.30			O1B
O2B			2.18	2.19				2.16							O2A
O3B						2.11					2.30				O2B
O3G						3.06									O3B
O G72			2.18					2.09							O G72
OE E89				2.24	2.22				1.99	2.45		2.72/3.06			OE E89
OE E93			2.13	2.19				2.05	2.10						OE E93
OE E150				2.37		2.03			2.39	2.98	2.26				OD D146
O4 ribose m^7G						3.17				2.49					OE E150
W505				2.12								2.60			W615
W633			2.20									2.99			W628
											2.86				W629

Entries in italics are Mn^{+2} in triad.
Mn305* and Mn306* are conditionally occupied sites in subunit B.
N, coordination number; Q, occupancy.
Approximately equivalent Mn^{+2} sites in the A and B subunits are: Mn300 = Mn304; Mn301 = Mn305; Mn302 = Mn306*; Mn303 = Mn306.

X29. The constellation of Mn^{+2} atoms in the active site of monomer A (Figure 6) presents a triad of Mn^{+2} juxtaposed to three oxygens of the P_β phosphoryl group of the m^7GpppA. This interaction occurs on the accessible face toward which inline attack of a nucleophile on P_β would occur in cleaving the P_β-P_α pyrophosphoryl linkage to release 5′-phosphoryl RNA as the leaving group. This triad could serve to both activate solvent to a nucleophile and also stabilize the trigonal pentacovalent transition state of the reaction. The fourth Mn^{+2} bridges the P_β-P_α scissile bond and could stabilize both the transition state and the 5′-P_α-phosphoryl-RNA leaving group. Alternatively, the same products (m^7GDP and 5′-P_α-phosphoryl-RNA) could be formed through nucleophilic attack on P_α of the m^7GpppA. However, the structure of the m^7GpppA complex with X29 argues against this latter mechanism for several reasons. The conformation around the P_β-P_α pyrophosphoryl group of the m^7GpppA provides no access for inline attack on P_α by a nucleophile. Also, only one of the oxygens of the P_α phosphoryl group is coordinated to an Mn^{+2}, and only this same single Mn^{+2} is close enough and in position to activate a water for attack on P_α. In contrast, the Mn^{+2} triad in monomer A provides three Mn^{+2} for nucleophile activation and transition state stabilization on an accessible face of the P_β phosphoryl group, consistent with inline attack as hypothesized for other nucleases. The fourth Mn^{+2} in each subunit (which is the same one noted above as a candidate to activate solvent for nucleophilic attack on P_α) bridges the P_β-P_α phosphoryl group, resembling bimetallic nucleases in which a metal is hypothesized to bridge the scissile bond, stabilizing charge accumulation in the transition state and in the leaving group (Steitz and Steitz, 1993).

We suggest that the Mn^{+2} triad observed in X29 serves four functions: activation of a water molecule for nucleophilic attack on P_β; stabilization of the negative charge developed on the phosphoryl oxygens in the transition state; stabilization of the 5′-phosphorylated RNA leaving group; and stabilization of the triphosphate group in a conformation susceptible to nucleophilic attack (Figures 6 and 7B). In the A site of X29, Mn302 and Mn303 have the lowest coordination numbers (2 and 3) and could function in concert to activate a water molecule to hydroxide nucleophile, as is postulated for bimetal enzymes. On the other hand, it is possible that the highly electropositive center created by the Mn^{+2} triad provides a gate which further activates hydroxide ion to a nucleophilic oxide, a possibility that has been proposed for a bimetal center (Williams et al., 1999). The combination of two or three metal electrophiles should facilitate deprotonation of a shared solvent (Aubert et al., 2004) relative to only one metal, but will also diminish the nucleophilicity of the resultant coordinated nucleophile (Williams et al., 1999). Both of these effects would be amplified in a trinuclear Mn^{+2} active site like that observed in the X29-m^7GpppA complex, but would be modulated by the interactions of the oxygens of the target phosphoryl group as the transition state is approached.

The stability of the m^7GpppA complex in the crystal may be a consequence of the incubation pH of 7.68, which is lower than the pH optimum for X29 decapping (8.0–9.0) (B.A.P., unpublished data) and lower than the pKa of a putative hydroxyl group. The high Mn^{+2} concentration used in the crystal complex structure could also retard cleavage of the bound m^7GpppA, as the Mn^{+2} concentration dependence of the decapping reaction shows a dropoff in activity at increasing Mn^{+2} concentrations below those used in the crystal complex. The requirement for a substantial part of the U8 snoRNA in order to observe gel shifts with X29 (Ghosh et al., 2004) suggests the possibility that subtle changes in structure of the RNA substrate or the enzyme are necessary for cap cleavage to occur.

A Role for RNA Substrate in Activating Apo-X29 to Holo-Enzyme

The binding of Mn^{+2} to apo-X29 only in the presence of nucleot(s)ide suggests that substrate ribonucleotide binding may be required for metal binding to form active holo-X29. Nucleotides bind Mn^{+2} and Mg^{+2} with high affinity, primarily through interactions with phosphoryl groups, and U8 snoRNA could carry metals as counterions into the active site of X29 upon binding. X29 crystals soaked with Mn^{+2} plus m^7GDP, m^7GTP, or m^7G bind the Mn^{+2} but without binding of the nucleot(s)ide. In the cases of the nucleotide soaks, the presence of pyrophosphate impurity competes with the nucleotide for coordination to bound Mn^{+2} and may stabilize the bound Mn^{+2}. Also, some of the Mn^{+2} positions for these complexes deviate significantly from those observed in the X29-m^7GpppA complex structure and may not permit coordination to bound m^7G nucleotide in its lowest energy conformation. These two effects, plus the paucity of interactions of the m^7G group with the protein, imply diminished affinity of the m^7G nucleotides for X29 and account for their absence in the electron density maps.

In the case of m^7G-promoted binding of Mn^{+2}, there is no pyrophosphate impurity and no anionic character to the nucleoside to account for Mn^{+2} binding. Nevertheless, the structure of the m^7GpppA + Mn^{+2} complex shows how even the m^7G nucleoside alone could deliver Mn^{+2} to the active site of X29. One Mn^{+2} in the A subunit active site of the m^7GpppA + Mn^{+2} complex is coordinated to the O1′ and O5′ of the m^7G nucleoside (Figure 4B). This coordination may provide sufficient affinity of Mn^{+2} for m^7G, even in the absence of anionic phosphoryl groups, to permit transfer of the Mn^{+2} to the enzyme. As in the cases of the m^7G nucleotides, the only interaction of the m^7G nucleoside group is through stacking of Phe49 on the ligand ribose (Figure 4B), which is unlikely to be sufficient to retain the nucleot(s)ide in the active site. In the structure of the m^7GpppA-X29 complex, the ligand and Mn^{+2} are coordinately bound to each other and to the protein in a conformation that is susceptible to catalysis. This extended configuration of interactions is missing in m^7G nucleot(s)ide soaks, and would lead to dissociation of the low-affinity carrier nucleot(s)ides on delivery of the high-affinity Mn^{+2} atoms.

Substrate Specificity and Mn^{+2} Binding to X29

The pppG and m^7GpppA complex structures show that most of the interactions of the cap moiety with X29 (Figures 5, 6, and 7A) occur through the pppA/G part of the substrate. The adenine or guanine ring lies in a crevice where it makes several hydrogen bond interactions. Comparison of the pppG complex with that for

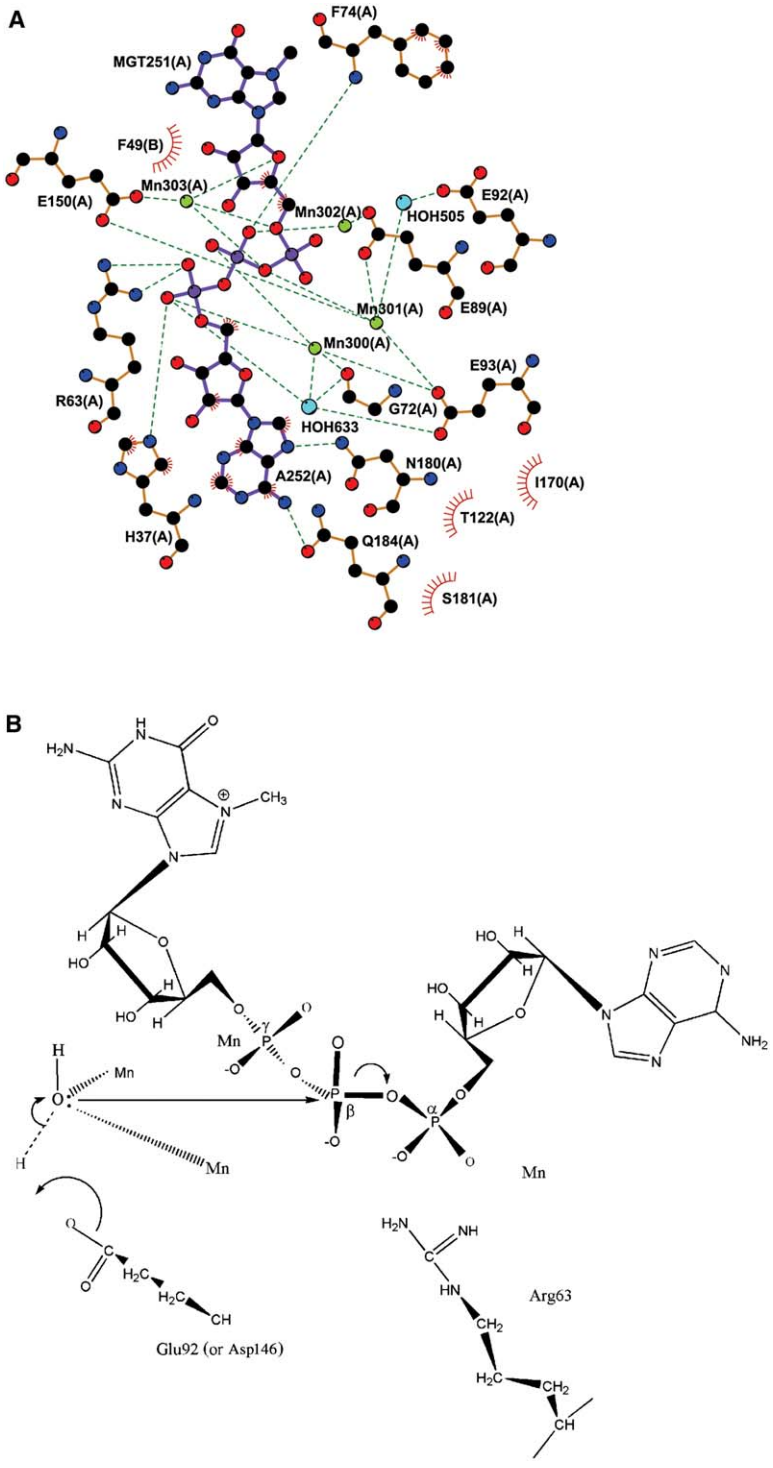

Figure 7. Ligplot Diagram of m^7GpppA Bound to the A Site of X29 and Hypothesized Mechanism for X29

(A) Coordination of the four Mn^{+2} atoms and hydrogen bond interactions of m^7GpppA are both shown as green dashed lines; hydrophobic interactions of m^7GpppA with protein ligands are shown by radiating arcs.

(B) The water molecule (or hydroxide anion) (left) is shown activated by two of the Mn^{+2} in the triad, and the side chain carboxylate of either Glu92 or Asp146 acts as proton acceptor. The resulting hydroxyl or oxide nucleophile axially attacks the P_β to form the pentacovalent trigonal bipyramid transition state. This transition state breaks down by cleavage of the distal axial P_β-O bond. The leaving group P_α-A… is stabilized by an ion pair to Arg63 and coordination to the fourth Mn^{+2}.

m^7GpppA shows that G makes four hydrogen bond interactions with the protein whereas A makes only two, suggesting that X29 may discriminate in favor of G at this position. It is possible that the syn conformation of A is an artifact of the abbreviated cap group used in this study, but an A modeled in the anti conformation makes even fewer hydrogen bond interactions with the protein than the syn. The in vitro transcribed RNAs used in our decapping assays have an m^7GpppG cap defined by the DNA template. However, the genomic sequence of functional U8 snoRNA genes indicates there may be an in vivo m^7GpppA form of U8 snoRNA (Peculis et al., 2001). For technical reasons, we have not tested whether X29 can decap an m^7GpppA form of U8 snoRNA in vitro.

Four of the six hydrogen bonds between the protein and A or G nucleobase in the cap are made by Gln184 and Asn180 side chains. The amido groups of these

two side chains are inferred to be flipped in the two structures to accommodate the alternative proton donors and acceptors on the A and G. These protein side chain determinants of substrate specificity are bifunctional and would not contribute to discrimination. From our two different complex structures, it is clear that either of these bases at this position can bind to X29, and the small difference in inferred affinity may reflect biological determinants, such as the relative abundance of different RNA substrates.

The m^7G and the ribose of A or G make few if any interactions with the X29 protein. This is consistent with the binding of uncapped U8 snoRNA to X29 (Ghosh et al., 2004) and implies that the m^7G makes little contribution to substrate binding or specificity. Similarly, putative methylation of the ribose 2′ hydroxyl groups of the A or G in vivo would have no effect on substrate binding, as this site makes no contact with X29 and is facing solvent.

As noted above, the configuration of Mn^{+2} atoms in the X29 active site that coordinate with the triphosphoryl group of the cap define a unique conformation for this polyanionic part of the substrate. This conformation sets up the target P_β for axial nucleophilic attack from the side where the Mn^{+2} triad lies. The requirement for this conformation along with the negligible contribution of the m^7G and the dominant contribution of the base on the 3′ side of the cap group can explain the paradoxical binding of pyrophosphate impurity rather than the more abundant nucleotides in the m^7GDP and m^7GTP soaks. In the absence of the constraining effects of the bound A (or G), the phosphoryl groups of the m^7GDP and m^7GTP nucleotides may not be in a favorable conformation for binding to X29 through coordination to the Mn^{+2} atoms. In contrast, the bound pyrophosphate exactly superposes on the P_α-P_β pyrophosphoryl groups of the m^7GpppA ligand and coordinates with several Mn^{+2} with almost identical geometry. This would stabilize the binding of these Mn^{+2} and explain the variability in the positions of the other Mn^{+2}.

The model of substrate-induced binding of metal cofactor to X29 may also confer other changes on the active site of X29 that are not visible from the crystal structures. The exceptionally dense cluster of carboxylate groups in the active site of apo-X29 may be stabilized by local hydration and is likely to have carboxylates with pKs perturbed to higher values. Binding of RNA substrate ligand carrying Mn^{+2} (or Mg^{+2}) may release bound solvent and lower the pKs of the carboxylate groups, thereby favoring binding of the metal presented on the ribonucleotide substrate. The observed changes in side chain orientation and the hypothesized changes in protonation state could account for the variability in position of the Mn^{+2} atoms in the active sites of X29 complexes with incomplete substrates and would support the notion that the substrate plays a role in imposing the correct catalytic and binding configuration on the active site metals and their ligands.

The variable distribution and number of metal sites may also be a consequence of the high concentrations (relative to in vivo levels) of Mn^{+2} used in our soaks and/or to the use of small nucleot(s)ide ligands rather than a larger RNA. The concentrations of Mn^{+2} used in our crystal soaking experiments are at least 100-fold higher than both the cellular concentrations of Mn^{+2} (Ash and Schramm, 1982) and the K_d determined from our Hill plot. These Mn^{+2} concentrations could lead to occupancy of lower affinity sites in the crystal soaks, for which no concentration dependence on Mn^{+2} was determined. The requirement for a nucleot(s)ide to observe Mn^{+2} binding in crystal soaking experiments makes comparison of our crystal conditions to the cellular concentrations problematic, because nucleot(s)ide concentration may be limiting. The K_d for Mn^{+2} binding in solution lies in the physiological range, but the higher in vivo concentrations of Mg^{+2} and its known specific association with RNA favor it as the metal cofactor of X29 in vivo.

Relationship to Other Cap Binding Proteins and In Vivo Function of X29

Like X29, the yeast (Dunckley and Parker, 1999) and human (Wang et al., 2002) mRNA decapping enzymes also have characteristic Nudix domain sequences. The recently determined crystal structure of yeast Dcp2p (She et al., 2006) confirmed that this domain has the Nudix fold. Available structures of other cap binding proteins show that the m^7G group binds in a well-defined site and makes interactions with the protein that define a specificity for the cap component of the substrate (Calero et al., 2002; Chen et al., 2005; Fabrega et al., 2004; Gu et al., 2004; Worch et al., 2005). The surprising lack of interactions between X29 and the m^7G nucleobase of the cap distinguishes it from these other cap binding proteins and is consistent with the failure of m^7GpppA or pppG to compete with capped RNA in the decapping reaction (B.A.P., unpublished data). X29 may have evolved different specificities from other cap recognition proteins to exclude interactions with m^7G and thereby prevent recognition and decapping of noncognate substrate RNAs. Such negative discrimination would impose selective restraints that may have led to the evolution of stronger specificity for other parts of the U8 snoRNA substrate distal to the 5′ terminus. The failure of truncated forms of U8 snoRNA consisting of the 5′ 40-nucleotide fragment or the 3′ 100-nucleotide fragment to compete effectively for binding to X29 against full-length U8 snoRNA indicates that higher order structure or multiple recognition sites in the sequence confer specificity and affinity on the X29-U8 snoRNA interaction.

We hypothesize that X29 is a negative regulator of cellular levels of U8 snoRNA and is itself regulated by product inhibition in its reaction. In our postulated mechanism, although the decapped U8 snoRNA product is the "leaving" group, it will very likely remain bound to the protein. In contrast, the weakly bound m^7GDP cap product is likely to dissociate, possibly carrying away the bound Mn^{+2} triad, leaving an uncapped U8 snoRNA-apo-X29 product complex (Figure 7B). This reaction pathway is consistent with the observation that uncapped U8 snoRNA binds to X29, even in the absence of added metal.

If cellular X29 is primarily bound as a product complex, then X29 may function both as a biosensor of U8 levels and as an enzyme. Our current solution assay for X29 decapping of U8 is a single turnover experiment, which does not permit us to infer affinity or kinetic

Table 3. Data Collection and Refinement Statistics

	Native	CH_3HgCl	$PbCl_2$	$PtEtNH_2$	$m^7G + Mn^{+2}$	$m^7GDP + Mn^{+2}$	$m^7GTP + Mn^{+2}$	$pppG + Mn^{+2}$	$m^7GpppA + Mn^{+2}$
Data Collection									
Resolution (Å)	26.8–2.1 (2.15–2.10)	27.5–2.7 (2.77–2.70)	26.6–2.5 (2.56–2.50)	26.9–2.10 (2.21–2.10)	29.97–2.70 (2.74–2.70)	29.9–2.6 (2.67–2.60)	23.5–2.45 (2.54–2.45)	38.74–2.45 (2.54–2.45)	46.17–2.10 (2.18–2.10)
R_{merge}	0.054	0.088 (0.237)	0.041 (0.187)	0.050 (0.408)	0.051 (0.358)	0.050 (0.433)	0.046 (0.365)	0.057 (0.343)	0.037 (0.380)
$I/\sigma(I)$	7.1 (2.1)	6.4 (3.2)	9.3 (4.0)	10.0 (1.8)	9.6 (2.2)	8.9 (1.8)	14.1 (3.1)	25.4 (6.9)	19.8 (4.4)
Completeness	99.7 (99.7)	98.4 (99.8)	99.7 (99.8)	98.4 (98.2)	99.9 (100.0)	99.8 (99.8)	99.4 (99.5)	91.9 (91.3)	99.9 (100.0)
Redundancy	6.8 (6.7)	3.3 (3.3)	7.5 (7.1)	7.0 (6.7)	6.9 (7.0)	6.9 (6.8)	3.5 (3.5)	11.34 (10.04)	6.92 (6.88)
Phasing power		1.318	0.666/1.716 (anomalous)	0.653					
Figure of merit	0.484								
Refinement									
Resolution (Å)	26.9–2.1				27.6–2.7	27.6–2.6	23.0–2.45	45.0–2.45	40.0–2.10
No. reflections	27,165				13,247	14,223	17,559	16,269	26,835
R_{work}/R_{free}	0.204/0.257				0.198/0.262	0.202/0.257	0.222/0.260	0.211/0.265	0.212/0.263
No. atoms									
Protein	3,073				2,928	2,905	2,922	2,955	2,932
Ligand/ion					5	14	23	68	111
Water	186				49	44	73	48	97
B factors									
Protein	38.69				67.15	60.93	63.03	52.26	58.59
Ligand/ion					74.10	61.29	64.52	56.78	76.65
Water	47.93				56.31	55.84	63.74	50.66	59.06
Ramachandran analysis (%)									
Favored/allowed	89.9/9.6				87.6/11.6	88.8/10.1	88.8/10.3	89.8/9.7	91.2/7.6
Rms deviations									
Bond lengths (Å)	0.010				0.020	0.012	0.018	0.018	0.014
Bond angles (°)	1.096				1.219	1.161	1.222	1.139	1.140

constants for the decapping reaction. In vivo, the relative cellular concentrations of X29 and U8 snoRNA (capped and uncapped) will determine the levels of apo-, holo-, and product-inhibited forms of X29 and of U8 snoRNA and their complexes. Interactions of X29 with other cellular components, particularly those in the U8 snoRNP, are likely to play roles in the turnover and recycling of X29 and/or U8 snoRNA.

Experimental Procedures

Crystallization and Soaked Complexes

Crystals of recombinant X29 in both the native and cysteine-alkylated (by treatment with iodoacetamide) forms were prepared as described (Peculis et al., 2004). The native X29 structure, heavy atom soaks, and complexes of X29 with m^7GpppA were determined from unalkylated crystals; soaks with $MnCl_2$ and other nucleot(s)ides were done with alkylated X29 crystals. Both forms have equivalent activity in decapping and gel shift assays. Electron density for the carboxamido group was visible on Cys120 and Cys174 in some cases, but apparently disordered in others. Heavy atom soaks were done in the same artificial supernatant as described, but with Tris substituted for HEPES buffer. Soaks with methylmercury chloride (CH_3HgCl) and platinum ethylenediamine ($PtEnNH_2$) were done by preparing a saturated solution of the heavy atom compound, spinning out solid, and diluting the supernatant 1:5 into artificial supernatant. Soak with lead chloride ($PbCl_2$) was done in 5 μM solution. Ligand complexes of nucleot(s)ides with $MnCl_2$ were formed by soaking native X29 crystals in supernatants that were 10 mM HEPES (pH 7.7), 3.75% PEG 6000. Soaks of m^7G, m^7GDP, and m^7GTP (Sigma) with $MnCl_2$ were done at concentrations of 5 or 10 mM $MnCl_2$ and 5 mM nucleot(s)ide overnight. Soaks of pppG (Sigma) and m^7GpppA (New England Biolabs) were done at 1 mM nucleotide and 2 mM $MnCl_2$ overnight. Analysis for pyrophosphate was done with the P_iPer assay kit (Molecular Probes).

Data Collection and Processing

Crystals were cryoprotected in their soak solution with glycerol incremented in 5% (v/v) steps with 10 min equilibration to a final glycerol concentration of 30%. Data were measured on flash-cooled crystals on either an RAxisII or RAxisIV image plate diffractometer (Molecular Structure Corporation) with Osmics optics at 40 kv and 20 ma. Full anomalous data sets were collected for the $PtEnNH_2$ and $PbCl_2$ heavy atom soaks and for all crystals soaked in $MnCl_2$ except $m^7GTP + Mn^{+2}$. Data were processed with MOSFLM (Leslie, 1992) or D*Trek (Pflugrath, 1999) and scaled with SCALA or D*Trek (Table 3).

Phasing, Model Building, and Refinement

Heavy atom sites were determined with SOLVE (Terwilliger and Berendzen, 1999), the derivatives having phasing powers: CH_3HgCl, 1.32; $PtEnNH_2$, 0.65; $PbCl_2$, 0.67 (1.72 anomalous). Phases (figure of merit = 0.48) were obtained with SHARP (de la Fortelle and Bricogne, 1991). Initial phases were improved by density modification with solvent flipping (Abrahams, 1997) as implemented in SOLVE.

For the apo-X29 structure, an initial model was obtained via automated tracing with ARP/WARP (Perrakis et al., 1999) and subsequently refined via alternating cycles of manual rebuilding into SigmaA-corrected $2F_o - F_c$ electron density maps with Xfit (McRee, 1999) and computational refinement in CNS (Brunger et al., 1998) and REFMAC5 (Murshudov et al., 1999). For all of the X29 complex structures, soaked crystals were isomorphous with the apo-X29 native crystals and their structures were determined by molecular replacement with the refined apo-X29 structure as initial model. This initial model was refined via rigid body refinement in CNS followed by alternating cycles of manual rebuilding in Xfit or O (Kleywegt and Jones, 1997). For the lower resolution structures, noncrystallographic symmetry restraints were imposed between structurally conserved regions of the two monomers in the asymmetric unit during simulated annealing in CNS. Manganese ions were placed based on peaks in anomalous difference Fourier maps, except for the $m^7GTP + Mn^{+2}$, where they were identified by occupancy and coordination. Occupancies for manganese ions were set initially based on the intensities of peaks in anomalous difference Fourier maps. In the refined structures, these occupancies were adjusted to make isotropic B factors for the bound manganese ions comparable to the B factors for their ligands and to minimize significant ($\pm 3\sigma$) peaks in $mF_o - dF_c$ difference Fourier maps (Table 3). Surface charge distributions were done by numerical solution of the Poisson-Boltzmann equation with the program DELPHI as implemented in the INSIGHT 2000 package (Accelrys, San Diego, CA). In this calculation the protein formal charge set, which corresponds to unit charges on Lys, Arg, Glu, and Asp residues, was used. Figures were rendered with RIBBONS (Carson, 1997) and LIGPLOT (Wallace et al., 1995).

Decapping Assay

Approximately 0.1 pmol cap-labeled U8 RNA (Ghosh et al., 2004) was incubated with 45 mM Tris (pH 8.5), 1.2 pmol X29 protein, and varying concentrations of $MnCl_2$ from 10 to 150 μM in 10 μM increments. The reaction was incubated for 30 min at 37ºC, spotted on a PEI TLC plate (Roche), and developed in 0.75 M $LiCl_2$ and 1 M formic acid. After developing, the plate was dried and exposed to a Fuji phosphorimage plate for quantitation. The percent decapping was quantitated from the number of counts of m^7GDP/total counts per lane. Under these conditions, 100 μM yielded 100% decapping of input U8 snoRNA.

Acknowledgments

B.A.P. had support from the NIH and H.T.W. from an NIH instrumentation grant.

Received: September 23, 2005
Revised: November 2, 2005
Accepted: November 4, 2005
Published: February 10, 2006

References

Abrahams, J.P. (1997). Bias reduction in phase refinement by modified interference functions: introducing the γ correction. Acta Crystallogr. D Biol. Crystallogr. *53*, 371–376.

Ash, D.E., and Schramm, V.L. (1982). Determination of free and bound manganese(II) in hepatocytes from fed and fasted rats. J. Biol. Chem. *257*, 9261–9264.

Aubert, S.D., Li, Y., and Raushel, F.M. (2004). Mechanism for the hydrolysis of organophosphates by the bacterial phosphotriesterase. Biochemistry *43*, 5707–5715.

Bailey, S., Sedelnikova, S.E., Blackburn, G.M., Abdelghany, H.M., Baker, P.J., McLennan, A.G., and Rafferty, J.B. (2002). The crystal structure of diadenosine tetraphosphate hydrolase from *Caenorhabditis elegans* in free and binary complex forms. Structure *10*, 589–600.

Bessman, M.J., Frick, D.N., and O'Handley, S.F. (1996). The MutT proteins or "Nudix" hydrolases, a family of versatile, widely distributed, "housecleaning" enzymes. J. Biol. Chem. *271*, 25059–25062.

Brunger, A.T., Adams, P.D., Clore, G.M., DeLano, W.L., Gros, P., Grosse-Kunstleve, R.W., Jiang, J.S., Kuszewski, J., Nilges, M., Pannu, N.S., et al. (1998). Crystallography & NMR system: a new software suite for macromolecular structure determination. Acta Crystallogr. D Biol. Crystallogr. *54*, 905–921.

Calero, G., Wilson, K.F., Ly, T., Rios-Steiner, J.L., Clardy, J.C., and Cerione, R.A. (2002). Structural basis of m7GpppG binding to the nuclear cap-binding protein complex. Nat. Struct. Biol. *9*, 912–917.

Carson, M. (1997). Ribbons. Methods Enzymol. *277*, 493–505.

Chen, N., Walsh, M.A., Liu, Y., Parker, R., and Song, H. (2005). Crystal structures of human DcpS in ligand-free and m7GDP-bound forms suggest a dynamic mechanism for scavenger mRNA decapping. J. Mol. Biol. *347*, 707–718.

Conyers, G.B., Wu, G., Bessman, M.J., and Mildvan, A.S. (2000). Metal requirements of a diadenosine pyrophosphatase from *Bartonella bacilliformis*: magnetic resonance and kinetic studies of the role of Mn^{2+}. Biochemistry *39*, 2347–2354.

de la Fortelle, E., and Bricogne, G. (1991). Maximum-likelihood heavy atom parameter refinement for multiple isomorphous replacement and multiwavelength anomalous difference methods. Methods Enzymol. *277*, 472–494.

Dismukes, G.C. (1996). Manganese enzymes with binuclear active sites. Chem. Rev. *96*, 2909–2926.

Dunckley, T., and Parker, R. (1999). The DCP2 protein is required for mRNA decapping in *Saccharomyces cerevisiae* and contains a functional MutT motif. EMBO J. *18*, 5411–5422.

Fabrega, C., Hausmann, S., Shen, V., Shuman, S., and Lima, C.D. (2004). Structure and mechanism of mRNA cap (guanine-N7) methyltransferase. Mol. Cell *13*, 77–89.

Gabelli, S.B., Bianchet, M.A., Bessman, M.J., and Amzel, L.M. (2001). The structure of ADP-ribose pyrophosphatase reveals the structural basis for the versatility of the Nudix family. Nat. Struct. Biol. *8*, 467–472.

Ghosh, T., Peterson, B., Tomasevic, N., and Peculis, B. (2004). *Xenopus* U8 snoRNA binding protein is a conserved nuclear decapping enzyme. Mol. Cell *13*, 817–828.

Glusker, J.P., Katz, A.K., and Bock, C.W. (2001). Two-metal binding motifs in protein crystal structures. Struct. Chem. *12*, 323–341.

Gu, M., Fabrega, C., Liu, S., Liu, H., Kiledjian, M., and Lima, C. (2004). Insights into the structure, mechanism, and regulation of scavenger mRNA decapping activity. Mol. Cell *14*, 67–80.

Kleywegt, G.J., and Jones, T.A. (1997). Model building and refinement practice. Methods Enzymol. *277*, 208–230.

Leslie, A.G.W. (1992). Recent changes to the MOSFLM package for processing film and image plate data. Joint CCP4 + ESF-EAMCB Newsletter on Protein Crystallography *26*, 27–33.

Lin, J., Abeygunawardana, C., Frick, D.N., Bessman, M.J., and Mildvan, A.S. (1997). Solution structure of the quaternary MutT-M^{2+}-AMPCPP-M^{2+} complex and mechanism of its pyrophosphohydrolase action. Biochemistry *36*, 1199–1211.

Maxwell, E.S., and Fournier, M.J. (1995). The small nucleolar RNAs. Annu. Rev. Biochem. *64*, 897–934.

McRee, D.E. (1999). XtalView/Xfit—a versatile program for manipulating atomic coordinates and electron density. J. Struct. Biol. *125*, 156–165.

Mildvan, A.S., Xia, Z., Azurmendi, H.F., Saraswat, V., Legler, P.M., Massiah, M.A., Gabelli, S.B., Bianchet, M.A., Kang, L.W., and Amzel, L.M. (2005). Structures and mechanisms of Nudix hydrolases. Arch. Biochem. Biophys. *433*, 129–143.

Murshudov, G.N., Vagin, A.A., Lebedev, A., Wilson, K.S., and Dodson, E.J. (1999). Efficient anisotropic refinement of macromolecular structures using FFT. Acta Crystallogr. D Biol. Crystallogr. *55*, 247–255.

Peculis, B. (1997). RNA processing: pocket guides to ribosomal RNA. Curr. Biol. *7*, R480–R482.

Peculis, B.A., and Mount, S.M. (1996). Ribosomal RNA: small nucleolar RNAs make their mark. Curr. Biol. *6*, 1413–1415.

Peculis, B.A., and Steitz, J.A. (1993). Disruption of U8 nucleolar snRNA inhibits 5.8S and 28S rRNA processing in the *Xenopus* oocyte. Cell *73*, 1233–1245.

Peculis, B.A., DeGregorio, S., and McDowell, K. (2001). The U8 snoRNA gene family: identification and characterization of distinct, functional U8 genes in *Xenopus*. Gene *274*, 83–92.

Peculis, B., Scarsdale, J.N., and Wright, H.T. (2004). Crystals of X29, a *Xenopus laevis* U8 snoRNA-binding protein with nuclear decapping activity. Acta Crystallogr. D Biol. Crystallogr. *60*, 1668–1669.

Perrakis, A., Morris, R., and Lamzin, V.S. (1999). Automated protein model building combined with iterative structure refinement. Nat. Struct. Biol. *6*, 458–463.

Pflugrath, J.W. (1999). The finer things in X-ray diffraction data collection. Acta Crystallogr. D Biol. Crystallogr. *55*, 1718–1725.

She, M., Decker, C.J., Sundramurthy, K., Liu, Y., Chen, N., Parker, R., and Song, W. (2004). Crystal structure of Dcp1p and its functional implications in mRNA decapping. Nat. Struct. Mol. Biol. *11*, 249–256.

She, M., Decker, C.J., Chen, N., Tumati, S., Parker, R., and Song, H. (2006). Crystal structure and functional analysis of Dcp2p from *Schizosaccharomyces pombe*. Nat. Struct. Mol. Biol. *13*, 63–70.

Steitz, T.A., and Steitz, J.A. (1993). A general two-metal-ion mechanism for catalytic RNA. Proc. Natl. Acad. Sci. USA *90*, 6498–6502.

Terwilliger, T.C., and Berendzen, J. (1999). Automated MAD and MIR structure solution. Acta Crystallogr. D Biol. Crystallogr. *55*, 849–861.

Tomasevic, N., and Peculis, B. (1999). Identification of a U8 snoRNA-specific binding protein. J. Biol. Chem. *274*, 35914–35920.

Tyc, K., and Steitz, J.A. (1989). U3, U8 and U13 comprise a new class of mammalian snRNPs localized in the cell nucleolus. EMBO J. *8*, 3113–3119.

Venema, J., and Tollervey, D. (1999). Ribosome synthesis in *Saccharomyces cerevisiae*. Annu. Rev. Genet. *33*, 261–311.

Wallace, A.C., Laskowski, R.A., and Thornton, J.M. (1995). LIGPLOT: a program to generate schematic diagrams of protein-ligand interactions. Protein Eng. *8*, 127–134.

Wang, Z., Jiao, X., Carr-Schmid, A., and Kiledjian, M. (2002). The hDcp2 protein is a mammalian mRNA decapping enzyme. Proc. Natl. Acad. Sci. USA *99*, 12663–12668.

Warner, J.R. (1990). The nucleolus and ribosome formation. Curr. Opin. Cell Biol. *2*, 521–527.

Watkins, N.J., Segault, V., Charpentier, B., Nottrott, S., Fabrizio, P., Bachi, A., Wilm, M., Rosbash, M., Branlant, C., and Luhrmann, R. (2000). A common core RNP structure shared between the small nucleolar box C/D RNPs and the spliceosomal U4 snRNP. Cell *103*, 457–466.

Watkins, N.J., Dickmanns, A., and Luhrmann, R. (2002). Conserved stem II of the box C/D motif is essential for nucleolar localization and is required, along with the 15.5K protein, for the hierarchical assembly of the box C/D snoRNP. Mol. Cell. Biol. *22*, 8342–8352.

Weinstein, L.B., and Steitz, J.A. (1999). Guided tours: from precursor snoRNA to functional snoRNP. Curr. Opin. Cell Biol. *11*, 378–384.

Williams, N.G., Takasaki, B., Wall, M., and Chin, J. (1999). Structure and nuclease activity of simple dinuclear metal complexes: quantitative dissection of the role of metal ions. Acc. Chem. Res. *32*, 485–493.

Woolford, J.L., Jr. (1991). The structure and biogenesis of yeast ribosomes. Adv. Genet. *29*, 63–118.

Worch, R., Niedzwiecka, A., Stepinski, J., Mazza, C., Jankowska-Anyszka, M., Darzynkiewicz, E., Cusack, S., and Stolarski, R. (2005). Specificity of recognition of mRNA 5′ cap by human nuclear cap-binding complex. RNA *11*, 1355–1363.

Accession Numbers

Coordinates and structure factors for apo-X29 and the five liganded complexes of X29 have been deposited with the RCSB with the following accession numbers: apo-X29 1U20; m^7G + Mn^{+2} 2A8P; m^7GDP + Mn^{+2} 2A8Q; m^7GTP + Mn^{+2} 2A8R; pppG + Mn^{+2} 2A8S; and m^7GpppA + Mn^{+2} 2A8T.